Physics of Fluids

Electro-osmosis modulated periodic membrane pumping flow and particle motion with magnetic field effects

Cite as: Phys. Fluids **34**, 092014 (2022); https://doi.org/10.1063/5.0111050
Submitted: 18 July 2022 • Accepted: 31 August 2022 • Published Online: 27 September 2022

D. S. Bhandari, Dharmendra Tripathi and O. Anwar Bég

Physics of Fluids ARTICLE scitation.org/journal/phf

Electro-osmosis modulated periodic membrane pumping flow and particle motion with magnetic field effects

Cite as: Phys. Fluids **34**, 092014 (2022); doi: 10.1063/5.0111050
Submitted: 18 July 2022 · Accepted: 31 August 2022 ·
Published Online: 27 September 2022

D. S. Bhandari,[1] Dharmendra Tripathi,[1,a)] and O. Anwar Bég[2]

AFFILIATIONS

[1]Department of Mathematics, National Institute of Technology Uttarakhand, Srinagar 246174, India
[2]Multi-Physical Engineering Sciences Group, Department of Mechanical and Aeronautical Engineering, SEE, Salford University, Salford, Manchester M54WT, United Kingdom

[a)]Author to whom correspondence should be addressed: dtripathi@nituk.ac.in

ABSTRACT

Theoretical studies of micro-electro-mechanical systems provide important insight into the mechanisms and optimization of such devices for a range of applications, including biomedical and chemical engineering. Inspired by emerging applications of microfluidics, unsteady viscous flow in a microchannel with periodic membrane pumping modulated by electro-magnetohydrodynamics is analyzed in a mathematical framework. The membrane kinematics induces the pressure inside the microchannel, where an electric field enhances the capability of the pumping flow rate. This model is formulated based on the Navier–Stokes equations, the Poisson equation, and the Maxwell electromagnetic equations and is further simplified using the lubrication approximations and Debye–Hückel linearization. The transformed dimensionless conservation equations under appropriate boundary conditions are analytically solved and the graphical results are illustrated through MATLAB (2019b) software. From the computational results, it is found that the Hartmann number enhances the fluid pressure uniformly throughout the microchannel, while the electric field parameter enforces the direction of the pressure-driven flow. The time-averaged flow rate exhibits a linear decay with axial pressure gradient, and it is strongly elevated with electric field parameter whereas it is weakly increased with electric double layer thickness parameter. It is further observed that the fluid is driven unidirectionally by the membrane contractions via a particle tracking simulation method. This study is relevant to provide the parametric estimation in designing the magnetic field-based microfluidics devices for microlevel transport phenomena.

NOMENCLATURE

A	Amplitude of membrane contraction
a	Half-length of the membrane
$\boldsymbol{B}$	Applied magnetic field $(0, B_0, 0)$
$\boldsymbol{E}$	Applied electrical field
e	Protonic charge
$\boldsymbol{F}$	Body force
J	Local ion current density
K_B	Boltzmann constant
L	Length of the microchannel
M	Shape of the membrane profile
n_0	Concentration of ions
p	Pressure of the fluid
Q	Volumetric flow rate
t	Time scale
T_a	Averaged temperature of the electrolyte solution
U_{e0}	Reference electro-osmotic velocity
$\boldsymbol{U_i}$	Velocity vector $(\boldsymbol{u}, \boldsymbol{v}, 0)$ of the fluid
$\overline{z}$	The valence of the ions

Greek symbols

ε	Permittivity of electromagnetic fluid
κ	Inverse electric double layer (EDL) thickness
λ	Width of the microchannel
μ	Viscosity of the fluid
ρ	Density of the fluid
ρ_e	Density of charged ions
σ	Electrical conductivity

ψ Stream function
Φ Electric potential
Φ_0 Zeta potential

Dimensionless parameter

E_T Electric field parameter
Re Reynolds number
$\boldsymbol{H_a}$ Hartmann number
δ Ratio of width to length of the microchannel

I. INTRODUCTION

Micro-electro-mechanical systems (MEMS) are being increasingly deployed in medical and bio-engineering applications due to their excellent integrated functionalities achievable in such systems. A micropump is one of the key features of these systems where an electric field can be used to enhance the pumping efficiency. Jeong *et al.*[1] have fabricated a mechanical sensitivity-based peristaltic micropump that achieves a maximum flow rate of about 0.36 μl/s. This is particularly relevant to optimize the transportation of separated cells, moving reagents to the separation/mixing chamber, drug transport, genomic DNA analysis through pneumatic microfluidic pumping,[2] and separation techniques in capillary electrophoresis.[3] Based on the characteristics of peristaltic pumping, Forouzandeh *et al.*[4] classified the fluid actuation induced by the peristaltic micropump (PMP). These studies have focused on wave propagation in the flow direction, which is referred to as the continuous-scheme PMP.[5,6] Despite their good efficiency, several challenges exist in designing micropumps to deliver consistently high flow rates as well as high-pressure drops.

To induce consistently high flow rates in microfluidic devices without loss of pressure drop, the deployment of external electric field gradients (electro-osmotic flow, i.e., EOF) has, therefore, become increasingly popular in micromechanical systems. Typically, electro-osmotic flow[7] involves the generation of an electric double layer (EDL) near the charged surface as a charged solid surface comes into contact with an electrolyte solution. Therefore, when an electric field is imposed, the EDL has induced a bulk fluid flow, which is referred to as electro-osmotic flow.[8] This non-mechanical mechanism has proven to be the most efficient mechanism for conveying small quantities (microvolumes) of fluids in microfluidic devices.[9] Most recently, some interesting studies[10–15] on electro-osmotic flow (EOF) have been presented in the literature, including EOF of viscoelastic fluids with slip-dependent zeta potential,[10] evolution from periodic to chaotic AC electro-osmotic flows,[11] fluid mixing in combined electro-osmotic and pressure driven transport,[12] EOF of viscoelastic fluids in an isosceles right triangular cross section,[13] EOF over high zeta potential modulated surfaces,[14] and energy efficiency analysis in oscillatory EOF.[15] These studies have addressed the effects of the zeta potential, EDL thickness, fluids properties, and geometrical properties for electro-osmotic flow.

Magnetohydrodynamics (MHD) is another key mechanism available for regulating natural transport phenomena and has also been implemented widely in the augmentation of biological flows.[16] MHD techniques, which involve the interaction of an applied magnetic field and electrically conducting fluid media, are also deployed in controlling hemodynamic circulation, biomagnetic tissue thermal therapy, cancer tumor treatment, etc.[17–19] Das *et al.*[20] developed a novel technique to separate particles-based size in narrow fluidic confinements by studying the combined effects of magnetophoretic and magnetohydrodynamic transport phenomena. According to Chakraborty and Paul,[21] a significant increase in volumetric flow rates can be accomplished with a low-magnitude magnetic field. Bhandari *et al.*[22] analyzed the hydromagnetic flow induced by the periodic membrane contraction in a two-dimensional finite length channel. In addition, some studies have also focused on the influence of induced magnetic fields in MHD flows.[23–25] These arise when the magnetic Reynolds number is sufficiently high to generate magnetic induction, and the flow distorts the magnetic field. With the combination of magnetic and electric fields, electromagnetohydrodynamics (EMHD) has become increasingly popular for more efficiently manipulated fluid flow in micromechanical systems.[26–29] In this regard, a computational fluid dynamics (CFD) simulation of the combined influence of electric and magnetic fields in regulating the peristaltic transport of physiological fluids in a microchannel was reported by Ramesh *et al.*,[30] in which the effects of the Hartmann number and EDL thickness on flow and pumping characteristics were studied. Prakash *et al.*[31] have considered the dual effects of the external electric and magnetic fields in regulating non-Newtonian fluids flow through peristaltic pumping and discussed the flow analysis under the effects of non-Newtonian parameters. The use of electromagnetohydrodynamic (EMHD) in precisely controlling peristaltic microflows has been demonstrated in these studies with applications, including limited dilution of samples, improved processing capabilities for separation purposes, etc. Most of the above-mentioned literature are based on the continuous-scheme PMP.

However, the discrete-scheme PMP can achieve greater reliability via microscale fabrication processes. In response to this essential mechanism, Aboelkassem and Staple[32] have proposed a bioinspired membrane pumping mechanism ("non-propagative" where at least two membranes that operate with time-lag) based on insect respiratory phenomena at the microscale. This bio-inspired mechanism has the potential for pumping the fluid more efficiently with high pressure generated via the periodic membrane motion. In another membrane model, Aboelkassem[33] proposed a single membrane contraction that operates in a "propagative" mode. Furthermore, Bhandari *et al.*[34] extended Aboelkassem's[33] model to consider couple stress fluids flow under active membrane propulsion. When working fluids are electro-conductive, the characteristics of membrane pumping may further be enhanced via an external electric field. Tripathi *et al.*[35] applied electro-osmosis in the membrane-based pumping model and analyzed the effects of zeta potential and EDL thickness. Heat transfer analysis with pressure and buoyancy forces for the membrane-based pumping flow model was investigated by Bhandari *et al.*[36] Thus far, the combined influence of electro-osmotic and magnetohydrodynamics in electro-conductive membrane pumping has not been examined.

In this paper, a novel mathematical model is developed to examine the unsteady flow of electroconductive fluids in a microchannel with periodic membrane pumping under the effects of magnetic and electric forces. Although some previous studies have considered the fluids flow in the microchannel under the combined effects of a transverse magnetic field and an axial electrical field,[26,27] but they have not addressed the discrete scheme PMP, i.e., the periodic membrane pumping mechanism. This is the main objective and novelty of the present investigation. The influences of key control parameters, i.e., the Hartmann number, EDL thickness, electric field parameter, etc., are presented graphically. Additionally, fluid particle trajectories inside the microchannel through the periodic membrane contractions are

also computed via a particle tracking simulation method. This study finds applications in hybrid lab-on-chip for an electro-magnetic microscale pumping process in biomedical sciences and health care.

II. PROBLEM FORMULATION

A. Geometric model of membrane pumping

The membrane pumping based flow regime is illustrated in Fig. 1, where the transverse magnetic field and applied electrical field are also considered to regulate the transient viscous flow in the microchannel. Membrane pumping is generated on the upper and lower walls of the microchannel. The membrane is periodically propagating over a complete contraction (compression and expansion phases) cycle. The membrane resumes the initial position after completing the contraction cycle and repeats the process without any external force. The mechanism of periodic membrane pumping is mathematically expressed in a cartesian coordinate system as (see Ref. 33)

$$h^*(x^*,\mathrm{t}^*)=\begin{cases}\dfrac{\lambda}{2}; & \text{if } x^*\in\left[-\dfrac{L}{2},-a^*\right)\cup\left(a^*,\dfrac{L}{2}\right],\\ \dfrac{\lambda}{2}+A\left(\left(\dfrac{x^*}{a^*}\right)^{2M}-1\right)^3\left(1-k_o^*x^*\cos(\pi f\mathrm{t}^*)\right)\sin^2(\pi f\mathrm{t}^*); & \text{if } x^*\in[-a^*,a^*],\end{cases}\tag{1}$$

where $h^*(x^*,\mathrm{t}^*)$ is the function of axial coordinate (x^*) and time (t^*), which represents the walls of the microchannel with amplitude of membrane contraction (A), k_o^* is optimized for the membrane profile, M is the shape of the membrane profile, and $f=(U_{e0}/L)$ is the frequency, where, and U_{e0} is the reference electro-osmotic velocity. The length of the membrane ranges in $a^*\in\left[-\frac{L}{2},\frac{L}{2}\right]$ based on the model of Aboelkassem,[33] where the length (L) of the microchannel is significantly larger than the width (λ).

B. Theory of an electromagnetic field

The Maxwell equation is composed of the electrical and magnetic effects, which is used to derive the Lorentz force charge per unit volume, and the local ion current density is expressed as

$$J=\sigma\left(\boldsymbol{E}+\left(\boldsymbol{U}_i^*\times\boldsymbol{B}\right)\right)\quad\text{(Local ion current density)},\tag{2}$$

where σ is the electrical conductivity that quantifies the magnitude of the electrical field $\boldsymbol{E}$ and the flow velocity $\boldsymbol{U}_i^*$ with the transverse magnetic field $\boldsymbol{B}=(0,B_0,0)$ that are proportional to the current density. The flow is simultaneously acted upon by a transverse magnetic field and an applied lateral electric field (out of the channel of flow) of strength E_Z. The body force $J\times\boldsymbol{B}$ can be derived with the help of Ohm's law as

$$\begin{aligned}J\times\boldsymbol{B}&=\sigma\left(\boldsymbol{E}+\boldsymbol{U}_i^*\times\boldsymbol{B}\right)\times\boldsymbol{B}\\&=\sigma(\boldsymbol{E}+(u^*i+v^*j+0k)\times\boldsymbol{B})\times\boldsymbol{B},\\J\times\boldsymbol{B}&=\sigma B_0E_z-\sigma B_0^2u^*.\end{aligned}\tag{3}$$

Additional forces are exerted along with the driving axial pressure gradient as a result of the electromagnetic volumetric force σB_0E_z and a retarding magnetohydrodynamic volumetric force $\sigma B_0^2u^*$. It is important to note that despite there is no electric field applied along the axis

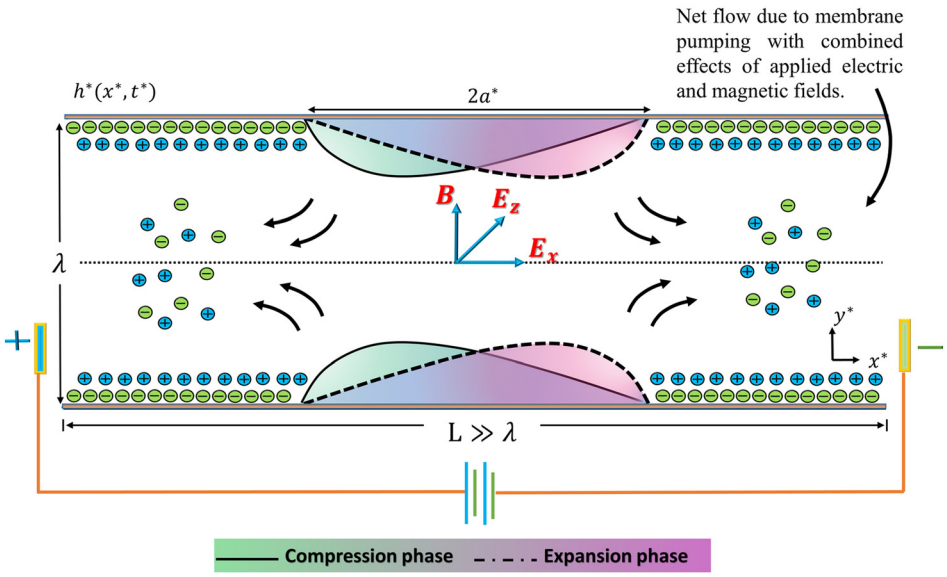

FIG. 1. Schematic diagram of the membrane-based pumping flow model modulated by electro-osmosis and magnetohydrodynamics.

of the channel, an electric field, specifically the streaming/electric potential field $E_x = \nabla\Phi^*$ is inherently induced by the advection of ionic species with the flow in the microchannel using the electrokinetic phenomenon.[21]

C. Electro-osmosis

In order to assess the electrokinetic phenomena in the microfluidic system, the attribute of the induced electric field is taken in terms of the electric potential (Φ^*). The advection of counter-ionic concentration with the flow due to the influence of an EDL forms near the liquid–wall interface, and an electric charge is deposited in the vicinity of the microchannel wall to enhance the potential at the walls. The charge density is measured by how much electric charge is accumulated in relation to the electric potential via the Poisson equation as

$$\nabla^2\Phi^* = -\frac{\rho_e}{\varepsilon}. \tag{4}$$

Here, ε is the permittivity of the electromagnetic fluid, and $\rho_e = e\bar{z}(n^+ - n^-)$ is the density of charged ions. e is the protonic charge, $\bar{z}$ is the valence of the ions, and $n^{\pm}$ are the number of cations and anions, respectively, which can be quantified by the Boltzmann distribution as $n_{\pm} = \mathrm{n_0}\exp(\mp\bar{z}e\Phi^*/\mathrm{k_B}T_a)$ and it is valid when the flow of the Peclet number is sufficiently small.[26] In such a case, the net charge density in a unit volume of the fluid is expressed as

$$\rho_e = 2n_0 e\bar{z}\sinh\left(\frac{e\bar{z}\Phi^*}{K_B T_a}\right), \tag{5}$$

where n_0 represents the concentration of ions in the bulk flow. K_B is the Boltzmann constant, and T_a is the average temperature of the electrolyte solution.

The parallel walls are assumed to be charged and bear a uniform zeta potential of Φ_0 at the wall, which is smaller than the thermal potential, i.e., $|\bar{z}e\Phi^*| < |k_B T_a| \rightarrow \Phi^* \ll 1$. Using the linear Debye–Hückel approximation, viz., $\sinh\left(\frac{e\bar{z}\Phi^*}{K_B T_a}\right) \approx \frac{e\bar{z}\Phi^*}{K_B T_a}$, the electric potential due to the presence of the EDL is described by the Poisson–Boltzmann equation that can be expressed as

$$\frac{\partial^2\Phi^*}{\partial x^{*2}} + \frac{\partial^2\Phi^*}{\partial y^{*2}} = -2n_0 e\bar{z}\left(\frac{e\bar{z}\Phi^*}{\varepsilon K_B T_a}\right), \tag{6}$$

subjected to the following boundary condition:

$$\Phi^*|_{y^*=h^*} = \Phi_0, \quad \left.\frac{\partial\Phi^*}{\partial y^*}\right|_{y^*=0} = 0. \tag{7}$$

D. Governing equations of the problem

The basic equations governed the electro-magneto-hydrodynamic (EMHD) flow driven by membrane-based pumping are expressed as

$$\nabla\cdot\boldsymbol{U_i^*} = 0, \tag{8}$$

$$\rho\left(\frac{\partial}{\partial t} + \boldsymbol{U_i^*}\cdot\nabla\right)\boldsymbol{U_i^*} = -\nabla p + \mu\nabla^2\boldsymbol{U_i^*} + \boldsymbol{F}, \tag{9}$$

where $\boldsymbol{F} = \rho_e E_x + J\times\boldsymbol{B}$ is the body force (combined effects of electric and magnetic cross fields acting on the fluids) and p is the fluid pressure. ρ and μ represent the density and kinematic viscosity of the fluid, respectively. The continuity, axial, and transverse momentum equations are expressed in the Cartesian coordinate system as

$$\frac{\partial u^*}{\partial x^*} + \frac{\partial v^*}{\partial y^*} = 0, \tag{10}$$

$$\rho\left(\frac{\partial u^*}{\partial t^*} + u^*\frac{\partial u^*}{\partial x^*} + v^*\frac{\partial u^*}{\partial y^*}\right) = -\frac{\partial p^*}{\partial x^*} + \mu\left(\frac{\partial^2 u^*}{\partial x^{*2}} + \frac{\partial^2 u^*}{\partial y^{*2}}\right) + \rho_e E_x + \sigma B_0 E_z - \sigma B_0^2 u, \tag{11}$$

$$\rho\left(\frac{\partial v^*}{\partial t^*} + u^*\frac{\partial v^*}{\partial x^*} + v^*\frac{\partial v^*}{\partial y^*}\right) = -\frac{\partial p^*}{\partial y^*} + \mu\left(\frac{\partial^2 v^*}{\partial x^{*2}} + \frac{\partial^2 v^*}{\partial y^{*2}}\right), \tag{12}$$

subjected to the following boundary conditions:

$$u^*|_{y^*=h^*} = 0, \quad v^*|_{y^*=h^*} = \frac{\partial h^*}{\partial t^*}, \quad p^*|_{x^*=L} = p_L, \quad \left.\frac{\partial u^*}{\partial y^*}\right|_{y^*=0} = 0, \quad v^*|_{y^*=0} = 0, \quad p^*|_{x^*=0} = P_0. \tag{13}$$

E. The non-dimensional variables

The Reynolds number is the ratio of the inertia force to the viscous force, and it can be defined as $Re = U_{e0}\rho\lambda/\mu$, where $U_{e0} = -\frac{\varepsilon\Phi_0 E_x}{\mu}$ is the reference electro-osmotic velocity. Introducing the following non-dimensional variables: $x = \frac{x^*}{L}, y = \frac{y^*}{\lambda}, t = \frac{t^* U_{e0}}{L}$, $h = \frac{h^*}{\lambda}, u = \frac{u^*}{U_{e0}}, v = \frac{v^*}{\delta U_{e0}}$, $p = \frac{p^*\lambda^2}{\mu U_{e0} L}, \Phi = \frac{ze\Phi^*}{k_B T}, \delta = \frac{\lambda}{L}, a = \frac{a^*}{L}$, and $\alpha_0 = \frac{A}{\lambda}$. The Poisson–Boltzmann Eq. (6) can be written as

$$\frac{\partial^2\Phi}{\partial y^2} = \kappa^2\Phi(y), \quad \kappa = \lambda\sqrt{\frac{2n_0 e^2\bar{z}^2}{K_B T_a\varepsilon}}, \tag{14}$$

where $1/\kappa$ represents the EDL thickness where κ is the ratio of the characteristic transverse length to the Debye length. With associative electric potential boundary condition $\Phi|_{y=h} = \Phi_0, \frac{\partial\Phi}{\partial y}|_{y=0} = 0$, the general closed-form analytical solution of Eq. (14) can be derived as

$$\Phi = \Phi_0\frac{\cosh(\kappa y)}{\cosh(\kappa h)}. \tag{15}$$

The volumetric net charge density ρ_e can be obtained in the form as

$$\rho_e = -\varepsilon\kappa^2\Phi_0\frac{\cosh(\kappa y)}{\cosh(\kappa h)}. \tag{16}$$

Introducing the non-dimensional variables in Eqs. (10)–(12) and employing the lubrication approximation, i.e., low Reynolds number ($Re \ll 1$) and width of the microchannel is much less than the characteristic length ($\lambda \ll L$), neglecting the nonlinear terms in the limits $\delta \ll 1$, and further substituting the expression for volumetric net charge density from Eq. (16), the reduced continuity and momentum equations are rewritten as

$$\frac{\partial u}{\partial x} + \frac{\partial v}{\partial y} = 0, \tag{17}$$

$$\frac{\partial p}{\partial x} = \frac{\partial^2 u}{\partial y^2} + \kappa^2 \frac{\cosh(\kappa y)}{\cosh(\kappa h)} + \boldsymbol{H}_a^2 E_T - \boldsymbol{H}_a^2 u, \quad \frac{\partial p}{\partial y} = 0. \tag{18}$$

The electromagnetic parameters arising in Eqs. (17) and (18) are as follows: $\boldsymbol{H}_a = B_0\,\lambda\sqrt{\frac{\sigma}{\mu}}$ is the Hartmann number, and $E_T = -\frac{E_z}{U_{e0}B_0}$ is the electric field parameter. In the axial momentum equation (18), the second term on the right-hand side represents the volumetric momentum generation caused by the electric potential, which is induced by the electro-osmotic flow. The third term represents the combined effect of the electrical and magnetic body forces, and the last term is the Lorentzian magnetic drag generated by the transverse magnetic field. From Eq. (18), it is inferred that the pressure is an independent function of y (i.e., $\partial p/\partial y = 0$) since terms of $O(Re\delta)$ and higher-order are neglected. The associated boundary conditions are reduced to the following forms:

$$\begin{aligned} &u|_{y=h} = 0, \quad v|_{y=h} = \frac{\partial h}{\partial t}, \quad p|_{x=L} = p_1, \\ &\left.\frac{\partial u}{\partial y}\right|_{y=0} = 0, \quad v|_{y=0} = 0, \quad p|_{x=0} = p_0. \end{aligned} \tag{19}$$

Equation (1) demonstrates the mechanism of periodically membrane propagation, i.e., compression and expansion phases of the membrane with spatial and temporal, respectively, are further represented in the non-dimensional form as

$$h(x,t) = \begin{cases} \frac{1}{2}; & \text{if } x \in \left[-\frac{1}{2}, -a\right) \cup \left(a, \frac{1}{2}\right] \\ \frac{1}{2} + \alpha_0 \left(\left(\frac{x}{a}\right)^{2M} - 1\right)^3 (1 - k_0 x \cos(\pi t))\sin^2(\pi t); & \text{if } x \in [-a, a]. \end{cases} \tag{20}$$

F. Analytical solutions

Solving the boundary value problem defined in Eqs. (17) and (18), the solution for the axial velocity is obtained as

$$\begin{aligned} u = {} & \frac{1}{\boldsymbol{H}_a^2}\left(\boldsymbol{H}_a^2 E_T - \frac{\partial p}{\partial x}\right)\left(1 - \frac{\cosh[\boldsymbol{H}_a y]}{\cosh[\boldsymbol{H}_a h]}\right) \\ & + \frac{\kappa^2}{\boldsymbol{H}_a^2 - \kappa^2}\left(\frac{\cosh[\kappa y]}{\cosh[\kappa h]} - \frac{\cosh[\boldsymbol{H}_a y]}{\cosh[\boldsymbol{H}_a h]}\right). \end{aligned} \tag{21}$$

By considering the continuity equation (17) and the axial velocity (21), the transverse velocity is derived as

$$\begin{aligned} v = {} & \frac{1}{\boldsymbol{H}_a^2}\frac{\partial^2 p}{\partial x^2}\left(y - \frac{\sinh[\boldsymbol{H}_a y]}{\boldsymbol{H}_a \cosh[\boldsymbol{H}_a h]}\right) \\ & - \left(E_T - \frac{1}{\boldsymbol{H}_a^2}\frac{\partial p}{\partial x}\right)\left(\frac{\sinh[\boldsymbol{H}_a y]\tanh[\boldsymbol{H}_a h]}{\cosh[\boldsymbol{H}_a h]}\right)\frac{\partial h}{\partial x} \\ & + \frac{\kappa^2}{\boldsymbol{H}_a^2 - \kappa^2}\left(\frac{\sinh[\kappa y]\tanh[\kappa y]}{\cosh[\kappa h]} - \frac{\sinh[\boldsymbol{H}_a y]\tanh[\boldsymbol{H}_a y]}{\cosh[\boldsymbol{H}_a h]}\right)\frac{\partial h}{\partial x}. \end{aligned} \tag{22}$$

Considering the transverse velocity subjected to the boundary condition (i.e., $v|_{y=h} = \frac{\partial h}{\partial t}$), a correlation between the membrane motion and the axial pressure gradient can also be obtained as follows:

$$\begin{aligned} \frac{\partial h}{\partial t} = {} & \frac{1}{\boldsymbol{H}_a^2}\frac{\partial^2 p}{\partial x^2}\left(\frac{\boldsymbol{H}_a h - \tanh[\boldsymbol{H}_a h]}{\boldsymbol{H}_a}\right) - \frac{\partial h}{\partial x}\left(E_T - \frac{1}{\boldsymbol{H}_a^2}\frac{\partial p}{\partial x}\right) \\ & \times \tanh^2[\boldsymbol{H}_a h] - \frac{\kappa^2}{\boldsymbol{H}_a^2 - \kappa^2}\left(\tanh^2[\boldsymbol{H}_a h] - \tanh^2[\kappa h]\right)\frac{\partial h}{\partial x}. \end{aligned} \tag{23}$$

Integration of Eq. (23) with respect to x, the pressure gradient is derived as

$$\begin{aligned} \frac{\partial p}{\partial x} = {} & \left\{ G_0(t) + \int_0^x \frac{\partial h(s,t)}{\partial t} ds - \frac{\kappa^2}{\boldsymbol{H}_a^2 - \kappa^2}\left(\frac{\tanh[\boldsymbol{H}_a h]}{\boldsymbol{H}_a} - \frac{\tanh[\kappa h]}{\kappa}\right) \right. \\ & \left. + E_T\left(\frac{\boldsymbol{H}_a h - \tanh[\boldsymbol{H}_a h]}{\boldsymbol{H}_a}\right) \right\}\left(\frac{\boldsymbol{H}_a^3}{\boldsymbol{H}_a h - \tanh[\boldsymbol{H}_a h]}\right). \end{aligned} \tag{24}$$

The pressure gradient is a function of both temporal coordinate (t) and axial coordinate (x), and $G_0(t)$ is calculated over the finite length of the microchannel as

$$\begin{aligned} G_0(t) = {} & \int_0^1 \frac{\boldsymbol{H}_a h - \tanh[\boldsymbol{H}_a h]}{\boldsymbol{H}_a^3} dx \left((p_1 - p_0) - \int_0^1 \frac{\boldsymbol{H}_a^3}{\boldsymbol{H}_a h - \tanh[\boldsymbol{H}_a h]} \right. \\ & \times \left(\int_0^x \frac{\partial h(s,t)}{\partial t} ds - \frac{\kappa^2}{\boldsymbol{H}_a^2 - \kappa^2}\left(\frac{\tanh[\boldsymbol{H}_a h]}{\boldsymbol{H}_a} - \frac{\tanh[\kappa h]}{\kappa}\right) \right. \\ & \left. \left. + E_T\left(\frac{\boldsymbol{H}_a h - \tanh[\boldsymbol{H}_a h]}{\boldsymbol{H}_a}\right) \right) dx \right). \end{aligned} \tag{25}$$

The pressure distribution is evaluated as

$$p = p_0 + \int_0^x \frac{\partial p(s,t)}{\partial x} ds. \tag{26}$$

The dimensionless stream function ($\psi = \int u dy - \int v dx$) is computed as

$$\psi = \left(\boldsymbol{H}_a^2 E_T - \frac{\partial p}{\partial x}\right)\frac{1}{\boldsymbol{H}_a^2}\left(y - \frac{\sinh[\boldsymbol{H}_a y]}{\boldsymbol{H}_a \cosh[\boldsymbol{H}_a h]}\right) + \frac{\kappa^2}{\boldsymbol{H}_a^2 - \kappa^2}\left(\frac{\sinh[\kappa y]}{\kappa \cosh[\kappa h]} - \frac{\sinh[\boldsymbol{H}_a y]}{\boldsymbol{H}_a \cosh[\boldsymbol{H}_a h]}\right). \quad (27)$$

The pumping flow is characterized by a volumetric flow rate $Q(x, t)$, which is a function of the pressure gradient. $Q(x, t)$ is calculated by integrating the axial velocity over the half width of the microchannel ($y = 0$ to $y = h$), which yields

$$Q = \left(\boldsymbol{H}_a^2 E_T - \frac{\partial p}{\partial x}\right)\frac{1}{\boldsymbol{H}_a^2}\left(h - \frac{\tanh[\boldsymbol{H}_a h]}{\boldsymbol{H}_a}\right) + \frac{\kappa^2}{\boldsymbol{H}_a^2 - \kappa^2}\left(\frac{\tanh[\kappa h]}{\kappa} - \frac{\tanh[\boldsymbol{H}_a h]}{\boldsymbol{H}_a}\right). \quad (28)$$

III. RESULTS AND DISCUSSSION

A. Parameter selection

The expressions derived for the flow characteristics in Sec. II are used to compute the axial velocity profile, pressure distribution, volumetric flow rate, and pumping characteristics at a fixed value of $M = 2, a = 0.2, \alpha_0 = 0.2,$ and $k_0 = 1.95$ and $t = T/4$ and $3T/4$. The influence of various parameters, such as the Hartmann number ($\boldsymbol{H}_a$), electrical field parameter (E_T), inverse EDL thickness (κ), and membrane shape parameter (M) on the above physical quantities, are visualized graphically by using MATLAB software. First, the permissible ranges of relevant physical parameters are defined. Here, the typical values of the sundry parameters for the microscale fluid flow with dynamic viscosity $\mu \sim 10^{-3}$ Pa s, the electric conductivity $\sigma \sim 2.2 \times 10^{-4}$ S m^{-1}, the applied magnetic field $\boldsymbol{B} \sim 0.018$–$0.44T$,[28] and the range of Hartmann numbers, i.e., $\boldsymbol{H}_a \sim 0$–8 are considered.[29] The potential of the applied electric field ranges as $\boldsymbol{E} \sim 0$–20 V/m, and the electro-osmotic velocity is taken as $U_{eo} \sim 100\ \mu$m/s. For the length L $\sim 300\ \mu$m and width $\lambda \sim 100\ \mu$m, the value of the inverse EDL thickness is considered as $\kappa \sim 1, 5, 10,$ and ∞.[27] An important limitation for microchannel flow is that the magnitude of the lateral electric field should not be too large, otherwise the induced transverse flow will not be neglected, which will contradict the assumption of unidirectional flow.[35] Therefore, the maximum magnitude of the electric field is taken up to 2.

B. Electric potential

The electric potential is crucial in diverse fields, including MEMS and technological processes at the microscale. The electric double layer (EDL) thickness is one of the most important characteristics of electro-osmotic flow, which affects the electric potential, physicochemical properties of electrolyte solutions, the extent of stability of colloidal systems, etc. The Poisson–Boltzmann theory helps us to understand the significance of the colloidal dispersions (i.e., zeta potential) and EDL thickness for the dispersion of the electric field. Figure 2(a) represents the influence of inverse EDL thickness (κ) on the electric potential. The electric potential (Φ) is slightly ascent with the order of κ, i.e., surface potential, which may cause either a decrease or an increase in the effective EDL thickness. However, $\kappa = \lambda\left(\frac{2n_0 e^2 \bar{z}^2}{K_B T_a \varepsilon}\right)^{1/2}$ increases the physical properties of the particle in the interfacial layer, which leads to the enhancement in the electric potential as shown in Fig. 2(a).

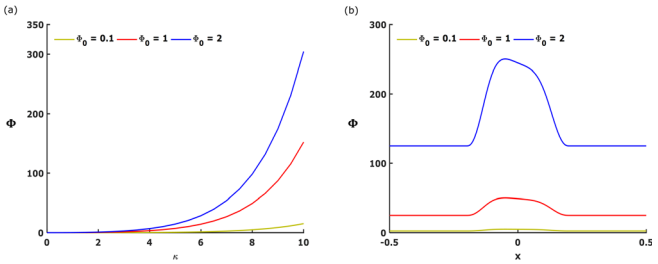

FIG. 2. The variation in the electric potential for different values of wall zeta potential with (a) the inverse EDL thickness and (b) the microchannel length.

Furthermore, the distribution of the electric potential across the microchannel for different values of zeta potential is sketched in Fig. 2(b). The uniform electric field is regulated in the microchannel except in the membrane region. This means that the electric potential increases as the wall surface interacts with the charged particles due to the membrane compression. On the other hand, the zeta potential provides excess charge due to the colloidal dispersion at the wall surface.

C. Pressure distribution in the membrane based microchannel

The contraction of the membrane in the upper half microchannel at fixed times $t = T/4$ is presented in Fig. 3. This membrane contraction profile generates the pressure (p) inside the microchannel in the range of $x \in [-0.2, 0.2]$, which can effectively propagate fluids in the microchannel. Corresponding to the membrane motion, the spatial variation in the fluid pressure (p) during the contraction phase ($t = T/4$) for different values of the sundry parameters is discussed through contour plots in Figs. 3 and 4. Moreover, the corresponding flow field of the velocity vector throughout the microchannel represents the direction of the flow. Here, it is observed that the fluid pressure is constant at each cross-sectional region within the microchannel. However, the kinematics of the periodic membrane generates uniform pressure distribution on both sides of the contraction region as shown in Fig. 3(a). The flow field of the velocity vector is stagnated at the center, which bifurcates the fluid in both directions.[34] In addition to the magnetic force, there is an opposing volumetric force of magnitude $\sigma B_0^2 u^*$, which acts to retard the axial pressure gradient. In Fig. 3(a), the Hartmann number ($\boldsymbol{H}_a = 5$) creates a strong Lorentzian force that controls the direction of the fluid velocity. Although the magnitude of the fluid pressure remains the same for the $\kappa = 3$ as presented in Fig. 3(b), the distribution of the fluid pressure is affected by the EDL thickness i.e., the axial pressure gradient is decreasing with the increase in the κ (i.e., reduction in the EDL thickness). The electrical field parameter ($E_T = 2$) enhances the velocity of the fluid, resulting in the decrease in the pressure after the mid-region. Physically, the influence of the magnetic force controls the strength of the flow, while the electric field enforces the direction of the flow field as shown in Fig. 4(a). The effect of the electric-magnetic fields in the thinner electric double layer is observed, mobilizing greater ionic diffusion, accelerating the pressure, and reducing the flow field as shown in Fig. 4(b). From this result, it is noted here that the membrane kinematics generates pressure inside the microchannel, while the Hartmann number controls the velocity

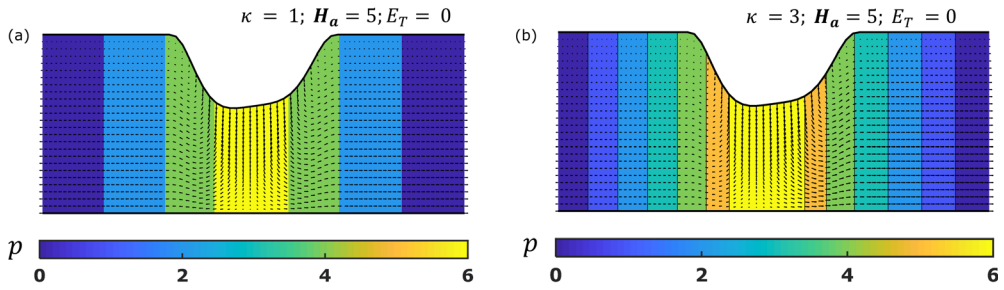

FIG. 3. The contour plot for distribution of pressure through the microchannel with a velocity vector flow field without the electric field: (a) $k = 1$ and (b) $k = 3$ at fixed values of $\boldsymbol{H_a} = 5$ and $M = 2$.

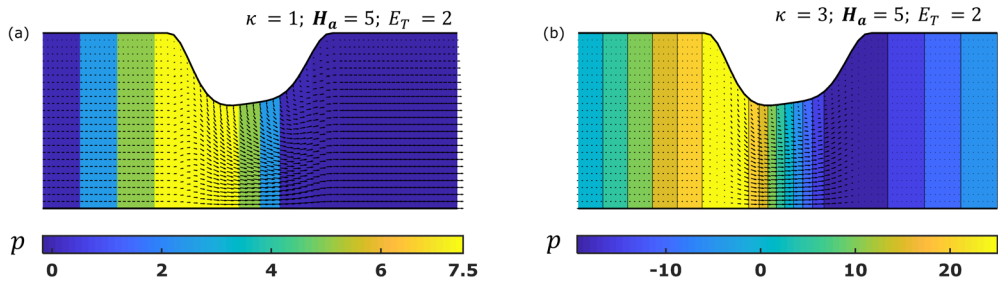

FIG. 4. The contour plot for distribution of pressure through the microchannel with a velocity vector flow field with the electric field: (a) $k = 1$ and (b) $k = 3$ at fixed values of $\boldsymbol{H_a} = 5$ and $M = 2$.

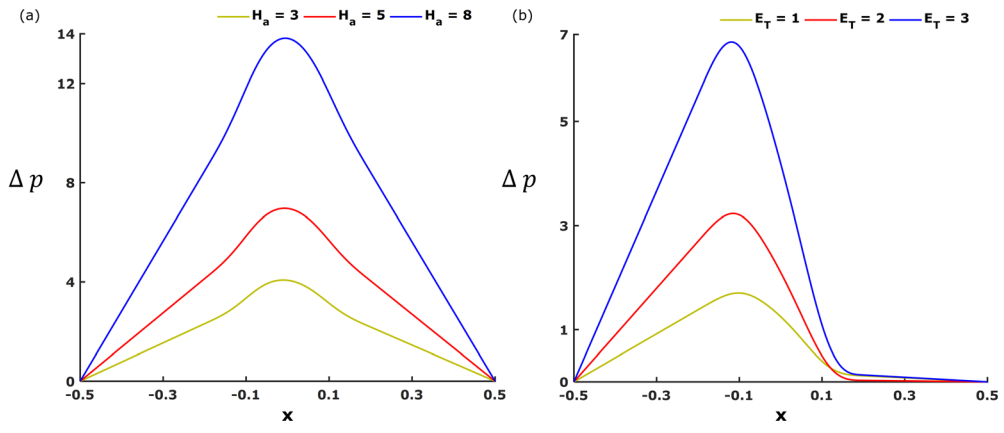

FIG. 5. The pressure distribution along the microchannel for different values of the (a) Hartmann number and (b) electric field parameter at fixed values of $t = T/4$, $\kappa = 1$, and $M = 2$.

of the fluid uniformly and the electric field enforces the direction of the flow while the EDL parameter improves the pressure-driven flow.

Figures 5(a) and 5(b) visualize the pressure distributions along the microchannel with different Hartmann numbers ($\boldsymbol{H_a}$) and electric field parameter (E_T) at time $t = T/4$. The pressure at the inlet and outlet of the microchannel is zero, and the maximum in the contraction region, i.e., $x \in [-0.2,\ 0.2]$ due to the membrane compression. In Fig. 5(a), the large value of the Hartmann number has raised the fluid pressure, particularly in the contraction domain as the magnetic force is maximum in this region. For the electric field ($E_T = 2$), the static pressure distribution is accumulated within the half region (i.e., $x \in [-0.5, 0]$). It suddenly decreases and attains the lowest value in the region $x \in [0,\ 0.5]$ as shown in Fig. 5(b). In addition, the Hartmann number increases the fluid pressure, i.e., a stronger magnetic field produces an accentuation in the magnetic pressure and distributes the uniform pressure throughout the microchannel. On the contrary, the transverse magnetic field regulates the pressure-driven flow and improves the efficiency of the mechanical system.

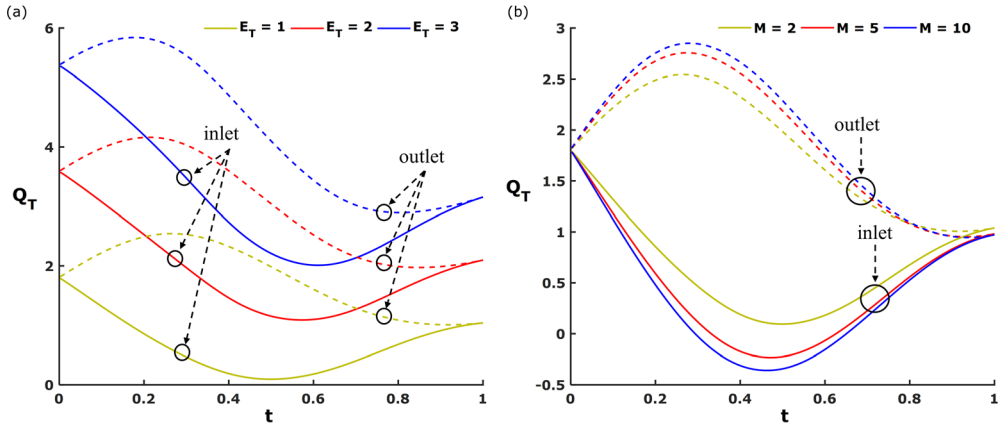

FIG. 6. Variation of the time-average flow rate across the length of the microchannel for different (a) electric field parameters and (b) membrane shape parameters at fixed values of $H_a = 3$ and $\kappa = 1$.

D. Pumping characteristics

Figures 6(a) and 6(b) depict the profiles for the time-averaged volumetric flow rate at the inlet and outlet positions for different values of the (a) electric field parameter and (b) membrane shape parameter with $H_a = 3$ and $\kappa = 1$. In the microchannel, as noted earlier, the periodic membrane motion produces the net flow, whereas the magnetic and electric parameters regulate the net flow. The result shown in Fig. 6 represents the time average flow rate (Q_T) at the inlet position $x = -0.5$ via the solid line and at the outlet position $x = 0.5$ via the dotted line. Identical results are attained at the inlet and outlet position over a complete contraction cycle in the opposite direction i.e., $Q_T(\text{inlet position},\ t = T/4) = Q_T(\text{outlet position},\ t = T/4)$. Higher magnitudes of the flow rate are produced consistently at the outlet (dotted lines) in both plots. Figure 6(a) shows that with an increase in the electric field parameter, there is a consistent augmentation in the flow rate. This is explained by the fact that larger values of E_T correspond to higher magnitudes of the axial driving force ($\sigma B_0 E_z$). However, an inspection of Fig. 6(b) indicates that greater values of the membrane shape parameter (M) increase the net flow rate only at the outlet, whereas at the inlet the opposite effect is generated, i.e., the flow rate is suppressed with increasing membrane shape parameter. Therefore, the membrane parameter exerts a very different effect on the transport phenomena depending on the location in the microchannel.

Figures 7(a) and 7(b) depict the time-averaged flow rate vs pressure gradient across the microchannel under the influence of the electric field parameter and the inverse EDL thickness at $t = T/4$ (compression phase). The plots indicate that the flow rate is inversely proportional to the pressure gradient, i.e., a high volumetric flow rate is attained for a small pressure gradient. From Fig. 7(a), it is evident that the Q_T is decreasing and becomes negative as the pressure gradient is increasing for $E_T = 1$, 2, and 3 (i.e., backward pumping flow can be possible due to the large pressure difference). However, the positive pumping ($Q_T > 0$) is enhanced and corresponds to the strongest electric field. In addition, the variation in the time-averaged flow rate as a function of the pressure gradient for three different cases (such as $\kappa = 1,\ 5,\ 10$) is shown in Fig. 7(b). It is noticed that the time averaged flow rate is increased with an increase in κ. A positive flow rate is only guaranteed for lower pressure gradient values at any value of κ.

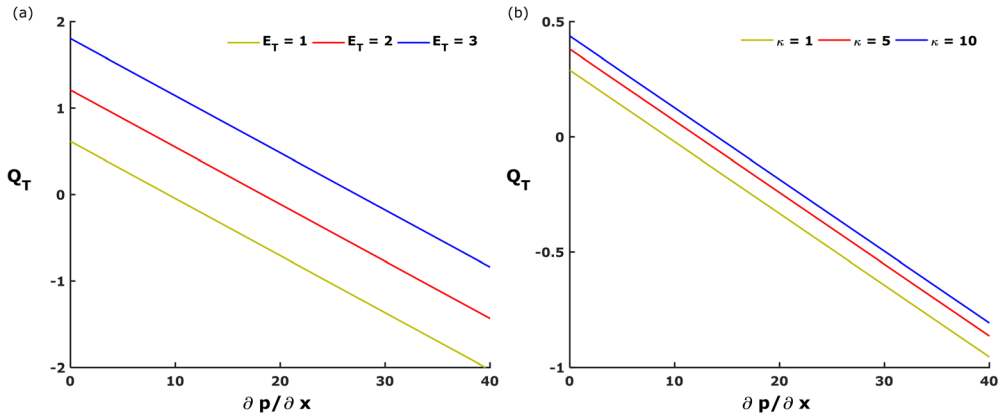

FIG. 7. Variation of the time-averaged flow rate for different (a) $E_T(= 1,\ 2,\ 3)$ and (b) $\kappa(= 1,\ 5,\ 10)$ at fixed value of $H_a = 3$ and $M = 2$.

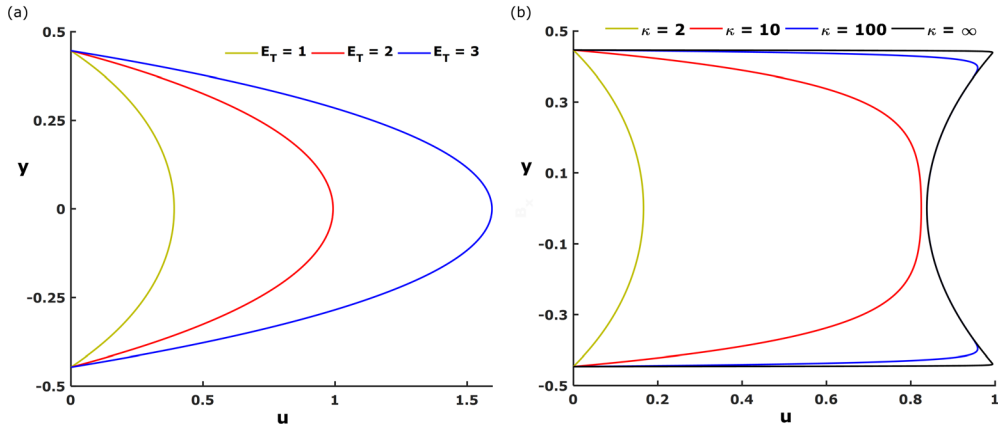

FIG. 8. The axial velocity throughout the microchannel for different values of (a) electric field parameter with $\kappa = 2$ and (b) inverse EDL thickness with $E_T = 2$ at fixed values of $H_a = 3$, $M = 2$, and $t = 3T/4$.

E. Velocity profile and flow field

Figures 8(a) and 8(b) represent the impact of the electric field parameter and inverse EDL thickness on the axial velocity profiles during the compression phase ($t = T/4$) at position $x = -0.1$. At the walls, the axial velocity is zero due to the no-slip boundary condition, and the maximum axial velocity of the fluid is achieved at the center of the microchannel. In addition, the electric field parameter enhances the movement of the fluid so that the axial velocity profile is increasing with the E_T as presented in Fig. 8(a). Here, the positive value of the axial velocity component indicates that the fluid is propelled in the forward direction. The κ changes the shape of the axial velocity component inside the microchannel (i.e., the aqueous fluid is inversely affected by the surface charge density of the EDL) as presented in Fig. 8(b). The high EDL thickness ($\kappa = 2$) ensures negligible electro-viscous effects, which lead to the axial velocity profile to remain parabolic. With reducing the EDL thickness, the shape of the velocity profile is shifting from parabolic to trapezoidal, and further, the magnitude of velocity is closer to the walls of the microchannel, which is distributed more uniform throughout the channel to maintain the controlled movement. When the EDL thickness is minimum ($\kappa \to \infty$), the trend of the velocity profile is further shifting from upward parabolic to downward parabolic since the electro-viscous effects are dominating as compared to the pressure force. It is also noteworthy that the axial velocity topology is the classical parabolic profile for $\kappa = 2$, whereas it evolves into a flattened plug-like profile for $\kappa = 5$, and thereafter for $\kappa = 10, \to \infty$ a sharp inverse parabola is computed in the core region, although the peak velocities for these two scenarios are indistinguishable at the central section of the microchannel, whereas slightly higher axial velocity is computed near the walls for $\to \infty$.

Physically, the magnetic force is proportional to $J \times B$, which clearly highlights the Lorentz force effect that resists the motion of fluid. For the large value of the Hartman number, the magnitude of the Lorentz force is high, and it leads to a small velocity in the microchannel. The minimum axial and transverse velocities magnitudes are attained for $\boldsymbol{H_a} = 3$ as shown in Figs. 9(a) and 9(b). The membrane propagation bifurcates the axial velocity in both left and right directions, while the transverse velocity is achieved near by the membrane domain. On the other hand, the thin EDL generates the high bulk concentration that permits a robust screening of the surface charge. From Fig. 10, it is observed that the electric potential is strong in the region near the wall, which leads to the increase in the axial velocity. The bolus is generated in the transverse velocity, which controls the movement of the fluid as sketched in Figs. 10(a) and 10(b). The electric body force is accumulated the axial velocity in the membrane domain with large magnitude. Furthermore, the nature of axial velocity remains consistent with the outward direction as presented in Fig. 11(a). Two positive and negative boluses are computed at the end of the membrane position as shown in Fig. 11(b). These results indicate that the dependence of the axial and transverse velocities on the value of E_T is much stronger than on the value of $\boldsymbol{H_a}$ and κ.

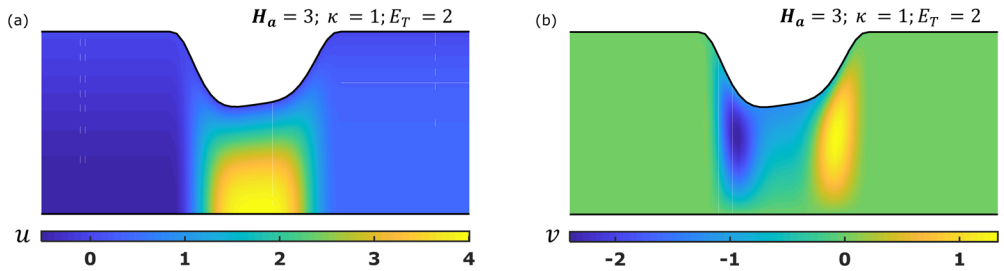

FIG. 9. The contour plot of the (a) axial velocity and (b) transverse velocity without the electric field for high EDL thickness ($\kappa = 1$).

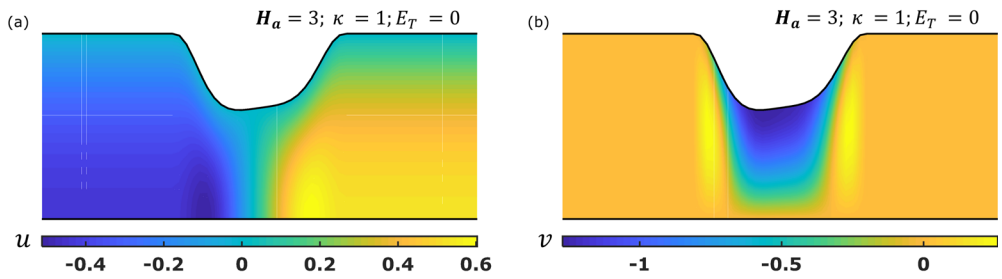

FIG. 10. The contour plot of the (a) axial velocity and (b) transverse velocity component without the electric field for low EDL thickness ($\kappa = 5$).

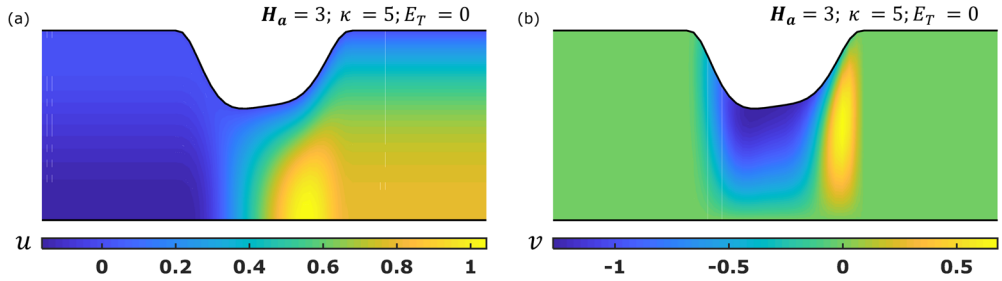

FIG. 11. The contour plot of the (a) axial velocity and (b) transverse velocity with the electric field for high EDL thickness ($\kappa = 1$).

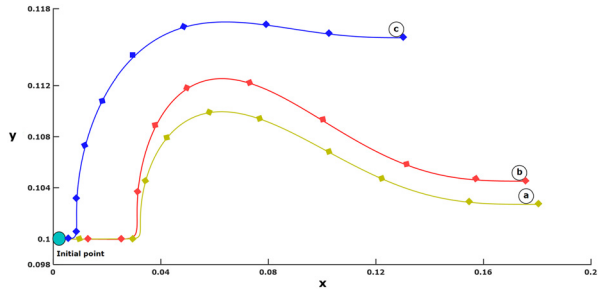

FIG. 12. Trajectory of a particle from an initial point for (a) $\kappa = 1;\ \boldsymbol{H_a} = 5; E_T = 0$, (b) $\kappa = 3; \boldsymbol{H_a} = 5; E_T = 0$, and (c) $\kappa = 3;\ \boldsymbol{H_a} = 5; E_T = 2$.

F. Particle tracking simulation

The particle tracking simulation method is applied based on the Lagrangian frame of reference as given in Eq. (29) to understand the instantaneous flow developed by the periodic membrane contractions inside the microchannel as depicted in Fig. 12 and mathematically defined as

$$\frac{d}{dt}\boldsymbol{X_p} = \boldsymbol{U_i}, \quad \boldsymbol{X_p}(0) = \boldsymbol{x}_0, \tag{29}$$

where $\boldsymbol{X_p}$ is the particle position vector and $\boldsymbol{x}_0$ describes the initial position of the particle. Here, it can be seen how the particle is propagated in the microchannel with rhythmic membrane contraction. In the case of no electric field, initially, the particle is constantly moving as shown in Fig. 12(a). However, the wave like movement in the particle is captured due to the membrane kinematics. This result illustrates that all the variables are linearly dependent on the applied pressure by membrane kinematics; however, the thin EDL thickness ($\kappa = 3$) is responsible for the small increment of the transverse direction as presented in Fig. 12(b). In order to highlight the combined effects of magnetohydrodynamic and electro-osmosis, the particle tracking results are plotted in Fig. 12(c). It is seen that the particle ascends rapidly and progresses as high up in the transverse direction.

IV. CONCLUSIONS

A mathematical model is presented for the viscous flow of electroconductive fluid in a microchannel, where the pressure is generated by periodic membrane pumping and further amplified by both magnetohydrodynamic and electro-osmotic effects. The discrete scheme PMP, i.e., the periodic membrane pumping mechanism, has been studied. The governing equations are derived for axial and transverse velocities, axial pressure gradient, and volumetric flow rate. The influence of key control parameters, i.e., Hartmann number (transverse magnetic field), inverse EDL thickness, and electrical field parameter are visualized graphically using MATLAB software. A particle tracking simulation method is also used to compute the instantaneous flow developed by the periodic membrane contractions inside the microchannel. The key findings of the present analysis are summarized as:

(i) The greater strength of the electric field elevates the net flow rate in the microchannel.
(ii) Time-averaged flow rate is increased with a decrease in the EDL thickness. A positive flow rate is only guaranteed for lower pressure gradient values at any value of κ.
(iii) The electric field has much efficiency to accelerate the fluid velocity rather than the inverse EDL thickness.

(iv) The magnetic parameter (H_a) enhances the fluid pressure uniformly throughout the microchannel, while the electric field parameter (E_T) enforces the direction of pressure-driven flow.
(v) The electric potential is strong in the region near the wall, which leads for the increase in the axial velocity.
(vi) The combined effect of electro-osmotic and magnetohydrodynamic elevates the particle to the transverse direction and moves forward.

This study has revealed some interesting insight into membrane pumping microsystems combined with the electromagnetohydrodynamic framework. However, attention has been confined to Newtonian ionic magnetic liquids. Future investigations may address non-Newtonian ionic magnetic liquid flow in the microchannel driven by periodic membrane pumping with thermal properties.

AUTHOR DECLARATIONS

Conflict of Interest

The authors have no conflicts to disclose.

Author Contributions

D. S. Bhandari: Conceptualization (equal); Methodology (equal); Software (equal); Writing – original draft (equal). **Dharmendra Tripathi:** Conceptualization (equal); Supervision (equal); Writing – review & editing (equal). **O. Anwar Bég:** Writing – original draft (equal); Writing – review & editing (equal).

REFERENCES

[1]O. C. Jeong, S. W. Park, S. S. Yang, and J. J. Pak, "Fabrication of a peristaltic PDMS micropump," Sens. Actuators, A **123–124**, 453–458 (2005).
[2]M. T. Taylor, P. Nguyen, J. Ching, and K. E. Petersen, "Simulation of microfluidic pumping in a genomic DNA blood-processing cassette," J. Micromech. Microeng. **13**(2), 201 (2003).
[3]M. Gong, N. Zhang, and N. Maddukuri, "Flow-gated capillary electrophoresis: A powerful technique for rapid and efficient chemical separation," Anal. Methods **10**(26), 3131–3143 (2018).
[4]F. Forouzandeh, A. Arevalo, A. Alfadhel, and D. A. Borkholder, "A review of peristaltic micropumps," Sens. Actuators, A **326**, 112602 (2021).
[5]T. Ma, S. Sun, B. Li, and J. Chu, "Piezoelectric peristaltic micropump integrated on a microfluidic chip," Sens. Actuators, A **292**, 90–96 (2019).
[6]V. Singhal, S. V. Garimella, and A. Raman, "Microscale pumping technologies for microchannel cooling systems," Appl. Mech. Rev. **57**(3), 191–221 (2004).
[7]D. Li, *Electrokinetics in Microfluidics* (Elsevier, 2004).
[8]N. A. Patankar and H. H. Hu, "Numerical simulation of electroosmotic flow," Anal. Chem. **70**(9), 1870–1881 (1998).
[9]N.-T. Nguyen, S. T. Wereley, and S. A. M. Shaegh, *Fundamentals and Applications of Microfluidics* (Artech House, 2019).
[10]K. N. Vasista, S. K. Mehta, S. Pati, and S. Sarkar, "Electroosmotic flow of viscoelastic fluid through a microchannel with slip-dependent zeta potential," Phys. Fluids **33**(12), 123110 (2021).
[11]Z. Hu, T. Zhao, W. Zhao, F. Yang, H. Wang, K. Wang, J. Bai, and G. Wang, "Transition from periodic to chaotic AC electroosmotic flows near electric double layer," AIChE J. **67**(4), e17148 (2021).
[12]B. Mahapatra and A. Bandopadhyay, "Efficacy of microconfined fluid mixing in a combined electroosmotic and pressure driven transport of complex fluid over discrete electrodes," Phys. Fluids **34**(4), 042012 (2022).
[13]X. Yang, S. Wang, M. Zhao, and Y. Xiao, "Electroosmotic flow of Maxwell fluid in a microchannel of isosceles right triangular cross section," Phys. Fluids **33**(12), 123113 (2021).
[14]B. Mahapatra and A. Bandopadhyay, "Numerical analysis of combined electroosmotic-pressure driven flow of a viscoelastic fluid over high zeta potential modulated surfaces," Phys. Fluids **33**(1), 012001 (2021).
[15]H.-F. Huang and K.-H. Huang, "Energy efficiency analysis of mass transport enhancement in time-periodic oscillatory electroosmosis," Phys. Fluids **33**(3), 032021 (2021).
[16]N. Pamme, "Magnetism and microfluidics," Lab Chip **6**(1), 24–38 (2006).
[17]A. Andreozzi *et al.*, "Modeling heat transfer in tumors: A review of thermal therapies," Ann. Biomed. Eng. **47**(3), 676–693 (2019).
[18]M. Suleman and S. Riaz, "3D *in silico* study of magnetic fluid hyperthermia of breast tumor using Fe_3O_4 magnetic nanoparticles," J. Therm. Biol. **91**, 102635 (2020).
[19]R. S. Chouhan *et al.*, "Magnetic nanoparticles—A multifunctional potential agent for diagnosis and therapy," Cancers **13**(9), 2213 (2021).
[20]S. Das, S. Chakraborty, and S. K. Mitra, "Magnetohydrodynamics in narrow fluidic channels in presence of spatially non-uniform magnetic fields: Framework for combined magnetohydrodynamic and magnetophoretic particle transport," Microfluid. Nanofluid. **13**(5), 799–807 (2012).
[21]S. Chakraborty and D. Paul, "Microchannel flow control through a combined electromagnetohydrodynamic transport," J. Phys. D **39**(24), 5364 (2006).
[22]D. S. Bhandari, D. Tripathi, and V. K. Narla, "Magnetohydrodynamics-based pumping flow model with propagative rhythmic membrane contraction," Eur. Phys. J. Plus **135**(11), 890 (2020).
[23]M. M. Bhatti, A. Zeeshan, and R. Ellahi, "Electromagnetohydrodynamic (EMHD) peristaltic flow of solid particles in a third-grade fluid with heat transfer," Mech. Ind. **18**(3), 314 (2017).
[24]K. S. Mekheimer, "Effect of the induced magnetic field on peristaltic flow of a couple stress fluid," Phys. Lett. A **372**(23), 4271–4278 (2008).
[25]N. S. Akbar, M. Raza, and R. Ellahi, "Influence of induced magnetic field and heat flux with the suspension of carbon nanotubes for the peristaltic flow in a permeable channel," J. Magn. Magn. Mater. **381**, 405–415 (2015).
[26]S. Sarkar, S. Ganguly, and S. Chakraborty, "Influence of combined electromagnetohydrodynamics on microchannel flow with electrokinetic effect and interfacial slip," Microfluid. Nanofluid. **21**(3), 56 (2017).
[27]D. Tripathi *et al.*, "Electro-magneto-hydrodynamic peristaltic pumping of couple stress biofluids through a complex wavy micro-channel," J. Mol. Liq. **236**, 358–367 (2017).
[28]K. Saha, P. V. S. N. Murthy, and S. Chakraborty, "Rheology-modulated alterations in electro-magneto-hydrodynamic flows in a narrow cylindrical capillary: Contrasting trends in high and low surface charge limits," Electrophoresis **43**(5–6), 732–740 (2022).
[29]A. Moradmand, M. Saghafian, and B. Moghimi Mofrad, "Electroosmotic pressure-driven flow through a slit micro-channel with electric and magnetic transverse field," J. Appl. Fluid Mech. **12**(3), 961–969 (2019).
[30]K. Ramesh, D. Tripathi, M. M. Bhatti, and C. M. Khalique, "Electro-osmotic flow of hydromagnetic dusty viscoelastic fluids in a microchannel propagated by peristalsis," J. Mol. Liq. **314**, 113568 (2020).
[31]J. Prakash, A. K. Ansu, and D. Tripathi, "Alterations in peristaltic pumping of Jeffery nanoliquids with electric and magnetic fields," Meccanica **53**(15), 3719–3738 (2018).
[32]Y. Aboelkassem and A. E. Staples, "A bioinspired pumping model for flow in a microtube with rhythmic wall contractions," J. Fluids Struct. **42**, 187–204 (2013).
[33]Y. Aboelkassem, "Pumping flow model in a microchannel with propagative rhythmic membrane contraction," Phys. Fluids **31**(5), 051902 (2019).
[34]D. S. Bhandari, D. Tripathi, and V. K. Narla, "Pumping flow model for couple stress fluids with a propagative membrane contraction," Int. J. Mech. Sci. **188**, 105949 (2020).
[35]D. Tripathi, V. K. Narla, and Y. Aboelkassem, "Electrokinetic membrane pumping flow model in a microchannel," Phys. Fluids **32**(8), 082004 (2020).
[36]D. S. Bhandari, D. Tripathi, and J. Prakash, "Insight into Newtonian fluid flow and heat transfer in vertical microchannel subject to rhythmic membrane contraction due to pressure gradient and buoyancy forces," Int. J. Heat Mass Transfer **184**, 122249 (2022).